Applied Surface Science 666 (2024) 160372

Contents lists available at ScienceDirect

Applied Surface Science

journal homepage: www.elsevier.com/locate/apsusc

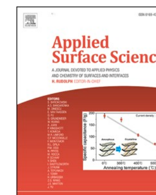

Full Length Article

Dynamics of phase transformations in Si and Ge upon strong excitation with UV femtosecond laser pulses

Daniel Puerto [a,b,*], Javier Solis [a], Jan Siegel [a,*]

[a] Laser Processing Group, Instituto de Óptica, IO-CSIC, Serrano 121, 28006 Madrid, Spain
[b] I.U. Física Aplicada a las Ciencias y las Tecnologías / Dept. Física, Ingeniería de Sistemas y Teoría de la Señal, Universidad de Alicante, 03690, San Vicente del Raspeig, Spain

A B S T R A C T

Femtosecond laser processing of semiconductors has evolved into a mature, high-precision fabrication technique, enabling a wide range of applications. While initially most studies have employed pulses at near infrared wavelengths, the interest in using UV laser pulses is constantly increasing due to the different excitation conditions as a consequence of the much shorter optical penetration depth, leading to an improved resolution. In this context, fundamental studies on the temporal dynamics of phase transformations triggered by such pulses are necessary in order to comprehend and eventually control the complex phase transformation pathways. Here, we report a detailed time-resolved study on the phase transformation dynamics of crystalline silicon and germanium upon irradiation with single 400 nm, 100 fs laser pulses in the moderate and high excitation regime. To this end, we have employed fs-resolved optical microscopy with a probe wavelength of 800 nm to study the reflectivity evolution of the irradiated surface over a temporal window ranging from 100 fs up to 20 ns. At moderate excitation fluence, the data reveals the entire sequence of laser-induced processes, starting from the generation of a free-electron plasma, non-thermal melting, ablation onset and expansion of a semi-transparent ablation layer with sharp interfaces. At excitation with peak fluences more than 30 times the ablation threshold, an anomalous transient high-reflectivity state is observed, which might be indicative of a recoil pressure-induced liquid–liquid phase transition. Moreover, 70 nm-thick amorphous surface layers are formed in both materials after irradiation at moderate fluences. Overall, our results provide relevant information on both, transformation dynamics and final state of both materials for fs-pulse excitation in the near-UV wavelength range.

1. Introduction

The prominent position of semiconductors amongst other material classes can be understood in part by their inherent ability to change their electrical conductivity upon a number of controllable external parameters, such as temperature, impurities, incident light and electrical voltage. Amongst them, silicon is the undisputed champion due to its abundance, followed by Ge amongst elemental semiconductors, together with GaN and other compound systems. The application outreach of these materials is not limited to the electronics industry but extends into the photonics sector in form of solar cells, lasers and integrated optical circuits, to name a few [1,2]. The existence of two structurally different solid phases of semiconductors, having very different physical and optical properties, further extends the range of applications they can be used for. Noteworthy, under certain conditions the phase can be switched upon irradiation with short and ultrashort laser pulses via melting followed by rapid resolidification [3]. This ability, discovered already in 1979, has led to an enormous research activity on the sub-class of so-called phase change materials aimed at optical and electrical data storage applications [4]. But also for silicon, laser-induced amorphization has been investigated since long and recently received renewed interest [5], also due to the prospect to write optical waveguides in form of amorphous surface channels [6]. Besides laser-induced amorphization or crystallization, laser ablation of semiconductors is of prime interest due to its presence in laser writing of surface structures with subwavelength feature sizes [7,8].

In order to obtain control over laser-induced material changes, time resolved optical techniques of the material response upon irradiation have proven to be powerful tools [9,10]. For the particular case of fs laser processing of semiconductors, the pioneering work by Shank and coworkers of optical probing the central region of a 620 nm fs laser excited spot Si with fs temporal resolution [11] was able to resolve the ultrafast phase transition to the liquid phase by recording the accompanying transient reflectivity changes. The same group developed a few years later a femtosecond imaging technique, in which they recorded a series of ultrafast snapshots of the sample surface on photographic film at given temporal delays [12], rather than simply recording the reflectivity values of the central region with a photodiode. Sokolowski-Tinten and co-workers employed a modernized version of this technique, employing a CCD camera, to unveil the peculiar ablation mechanism in

* Corresponding authors.
E-mail addresses: dan.puerto@ua.es (D. Puerto), j.siegel@csic.es (J. Siegel).

https://doi.org/10.1016/j.apsusc.2024.160372
Received 13 November 2023; Received in revised form 26 April 2024; Accepted 22 May 2024
Available online 28 May 2024
0169-4332/© 2024 The Author(s). Published by Elsevier B.V. This is an open access article under the CC BY-NC-ND license (http://creativecommons.org/licenses/by-nc-nd/4.0/).

silicon and other semiconductors and metals upon irradiation at 620 nm at moderate fluences. With this technique, ablation manifests as an expansion of a thin, semitransparent layer, giving rise to Newton rings caused by interference of the probe light at the different interfaces [13]. A similar study, revealed the presence of Newton rings also upon excitation at 800 nm wavelength [8]. Also for the case of Ge, several time-resolved studies upon irradiation at 800 nm exist [14,15], showing a qualitatively similar dynamics to the one observed for Si for low and moderate fluences. Yet, to the best of our knowledge there is only one work on time-resolved studies of Si at UV wavelengths. Izawa et al reported fs microscopy results upon excitation at 258 nm in the melting regime below the ablation threshold, reporting maximum melt durations of less than 1 ns [16]. Here, we report a complete study of the excitation, melting, ablation and resolidification dynamics upon irradiation of Si and Ge at 400 nm, 100 fs, measured with fs microscopy up to delays of 20 ns.

2. Experimental

The samples used here were polished ⟨1 0 0⟩ crystalline Si and Ge wafers. Before irradiation, ultrasonic bath cleaning in acetone and ethanol was performed but no attempt was made to remove the native oxide layer of ≈ 3 nm thickness. The experiment employs an amplified Titanium Sapphire system, providing a 1000 Hz pulse train of 120 fs laser pulses at 800 nm, used for sample irradiation and in-situ time-resolved reflection microscopy. A sketch of the experimental setup is shown in Fig. 1. Briefly, a shutter selects single pulses that are split into two pulses by means of a polarizing beam splitter. One fraction of the pulse is used for sample excitation at an angle of incidence of $\theta = 54^\circ$ and p-polarization, after having been frequency-doubled to $\lambda_{pump} = 400$ nm (removing the remaining fundamental frequency with a bandpass filter), which shortens the pump pulse to approximately 100 fs. The Gaussian elliptical $1/e^2$ spot – diameter at the sample surface after focusing with a 150 mm focal length lens was determined as $d_x = 2{\cdot}w_{0,x} = 62$ µm and $d_y = 2{\cdot}w_{0,y} = 36$ µm using the method proposed by Liu [17]. The peak fluence values given in this work have been calculated using the relation $F = 2{\cdot}E/(\pi{\cdot}w_{0,x}{\cdot}w_{0,y})$, with E being the laser pulse energy. The main reason for a non-normal incidence of the pump beam is to prevent the specular reflection of the pump beam to reach the CCD camera. The long pass filter we use to prevent pump light to reach the CCD is sufficient for the low intensity pump scatter but not for a specular reflection of a pump beam at the high fluences used.

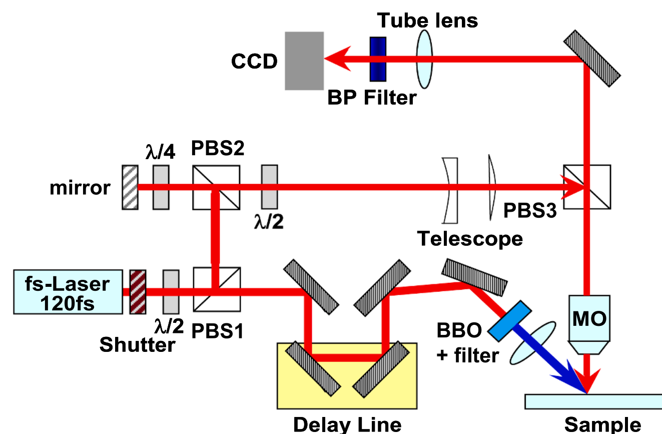

Fig. 1. Scheme of the experimental setup for single pulse irradiation monitored in-situ with fs microscopy. The abbreviations of the different components are as follows: Half-wave plate (λ/2); quarter-wave plate (λ/4); polarizing cube beam splitters (PBS1, PBS2, PBS3); beta barium borate frequency doubling crystal (BBO); microscope objective (MO); bandpass filter (BP). The full delay range (from −30 ps to 20 ns) can be accessed by means of a motorized delay line (1 ns with high resolution) in the pump beam line and a coarse manual delay in the probe beam arm (20 ns in steps of 2 ns).

The other fraction of the laser pulse is used to probe the laser irradiated region at normal incidence. To this end, the second fraction of the 800 nm pulse is used as an illumination source ($\lambda_{probe} = 800$ nm), by sending it through a combination of two waveplates (λ/4 and λ/2) and polarizing beam splitters (PBS1 and PBS2), together with a beam expanding telescope into the illumination port (PBS3) of a home-built optical microscope (composed of a 20x long working distance objective lens (NA = 0.40) and a 200 mm tube lens). The pulse energy of the probe pulse incident on the sample was constant for all experiment, below 2 µJ for both probing wavelengths (800 nm in the results shown in main manuscript and 400 nm in the results shown in the supplemental information). Considering that the illumination of the sample is designed to obtain a homogeneous field of view of the microscopy setup with the 20x objective lens (310 x 220 µm), the estimated waist of the Gaussian illumination profile was > 600 µm. This leads to a peak fluence of < 0.4 mJ/cm^2, well below excitation levels that could contribute to the material transformation. The reflected probe pulse light forms an image onto a 12 bit CCD camera. The pump–probe delay can be changed with fs resolution by moving a motorized optical delay line inserted in the pump beam arm. The delay range that can be accessed that way is 1 ns. In addition, longer pump–probe delays (up to 20 ns) have been accessed by changing manually the position of the mirror next to the λ/4 waveplate, thus lengthening the optical delay of the probe beam. Temporal overlap of pump and probe pulses has been achieved by placing a two-photon absorption photodiode at the sample position, reducing the pulse energies of the two beams such that no signal was generated by an individual beam, then scanning the motorized delay line until a signal was obtained.

For the experiment, a non-irradiated surface area is used for each delay value and three different images are acquired: Image 1, acquired before irradiation blocking the pump beam, is used for normalization purposes. Image 2, acquired at the desired pump–probe delay upon irradiation with the pump beam unblocked, is used to obtain the state of the surface during the ablation/modification process. Image 3, acquired at a very long delay (seconds) after irradiation with the pump beam blocked, is used to obtain the state of the surface after irradiation. That way, for each delay value two normalized reflectivity 32-bit images are obtained; one corresponding to the chosen delay value (obtained by dividing Image 2 by Image 1) and one corresponding to the final state after irradiation (obtained by dividing Image 3 by Image 1). In these images, pixel values of 1.00 correspond to the reflectivity of the pristine material surface. Zero delay between pump and probe pulse has been defined by assigning to the first image with a weak reflectivity increase above noise level a delay of + 100 fs. That way, it is possible to represent the data on a logarithmic time scale, which is important in order to be able to cover the enormous temporal window investigated.

The observed transient and permanent reflectivity changes can be related to the different phases (crystalline, amorphous and liquid) of each material with its characteristic optical properties (taken from Ref. [18]), as shown in Table 1. To this end, the relative reflectivity changes have been modeled as a function thickness of a surface layer (liquid or amorphous) on top of a crystalline material. The optical model used takes into consideration the fully coherent superposition of Fresnel reflections at all interfaces [air/liquid(amorphous) and liquid(amorphous)/crystalline] for the probe wavelength 800 nm at normal incidence (and at 400 nm for the data shown in the supplemental information).

The presence of the thin oxide top layer on Si and Ge and its possible influence on the data analysis and interpretation has been investigated. The corresponding oxides are non-absorbing (k = 0 for both materials) at the two wavelengths and have a rather low refractive index (SiO_2: n (400 nm) = 1.47 and n(800 nm) = 1.45; GeO_2: n(400 nm) = 1.64 and n (800 nm) = 1.60). Together with its small thickness (3 nm), the effect of the oxide layer on the reflectivity changes is very small (less than 2 % of the initial reflectivity as shown for Ge in Ref. [14]) and therefore also on

Table 1
Optical and thermal properties of Si and Ge at the two laser wavelength values used. The optical properties have been taken from [19] and [20].

	λ (nm)	Si	Ge
$n_{crystalline}$	400	5.570	4.141
	800	3.692	4.684
$k_{crystalline}$	400	0.387	2.215
	800	0.007	0.316
$n_{amorphous}$	400	4.270	3.420
	800	3.895	4.736
$k_{amorphous}$	400	2.200	2.831
	800	0.109	1.133
n_{liquid}	400	2.216	1.805
	800	4.162	4.036
k_{liquid}	400	4.664	4.249
	800	5.714	6.710
Thermal conductivity solid (W/m·K)		149	60
Thermal conductivity liquid (W/m·K)		57	43
Melting point T_m (K)		1687	1211
Boiling point T_b (K)		3538	3106

the energy coupling efficiency.

3. Results and discussion

3.1. Transformation threshold determination in Si and Ge upon irradiation at 400 nm, 100 fs

For both materials, we have performed at λ_{pump} = 400 nm single pulse irradiation series at increasing fluences, from below the amorphization threshold until two to three times the ablation threshold in order to determine the beam waist values $w_{0,x}$ and $w_{0,y}$ of the 2D Gaussian intensity distribution at the sample plane, using the method proposed by Liu [17]. The obtained values are listed in the experimental section. Now, it is straight-forward to determine for any peak fluence precisely the local fluence at any position within the irradiated region, by calculating the local intensity of the known 2D Gaussian intensity distribution, using the expression $F(x) = F\cdot\exp(-2x^2/w_{0,x}^2)$ for local positions along the horizontal x-axis [21]. We have exploited this relation in order to determine the two characteristic transformation thresholds in both materials, namely amorphization, which manifests by a reflectivity increase [6,22], and ablation, which manifests by the formation of a crater with a sharp ring. Fig. 2 shows optical microscopy images of single pulse irradiated region in Si and Ge at very similar peak fluences above the ablation threshold. In both images, a characteristic reflectivity increase due to amorphization and a sharp inner ablation crater can be appreciated, which allows a precise positioning of the respective threshold of each process, included in the figure as dashed lines to mark the horizontal position. The strong reflectivity increase due to the formation of a thin amorphous surface layer upon laser irradiation has been observed since long [5,6,22,28,29] and is due to the very different optical properties of the crystalline and amorphous phase. This layer is investigated in more detail for both materials in Section 3.3.

The respective position has been converted into local fluence to yield the threshold fluence for amorphization F_{am} and for ablation F_{abl}, whose values are displayed in Table 2. The table includes threshold values for normal incidence, extrapolated by considering the angle- and polarization-dependent reflectivity of both materials using the relation [23]: $F(0^\circ) = F(54^\circ)\cdot C_{angle}$, with $C_{angle} = [1 - Rp(54^\circ)] / [1 - Rp(0^\circ)]$, with Rp corresponding to the reflectivity for p-polarized light, yielding C_{angle}(Si) = 1.28 and C_{angle}(Ge) = 1.34. For Ge, these values are, to the best of our knowledge, the first reported values for fs laser irradiation at 400 nm. For the case of Si, they can be compared to the results reported by Izawa et al. [16], who reported threshold values at normal incidence for amorphization of ≈ 60 mJ/cm^2 and ≈ 160 mJ/cm^2 for ablation, which are in reasonable agreement with our values extrapolated to normal incidence (see Table 2).

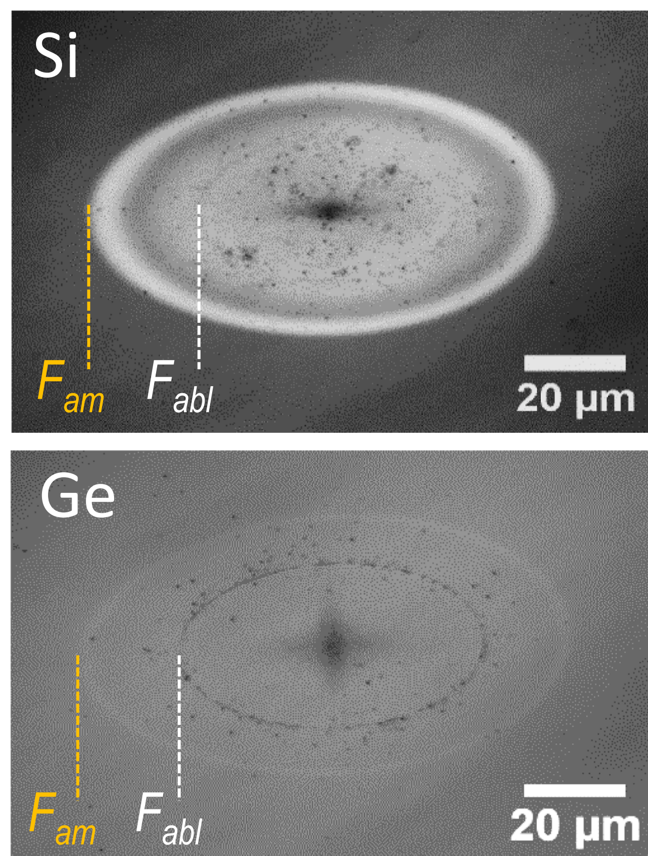

Fig. 2. Optical microscopy images upon illumination at 460 nm wavelength of the material surface after irradiation with single 400 nm, 100 fs pulses. (a) Si at F = 320 mJ/cm^{2}and (b) Ge at F = 340 mJ/cm^2. The dashed vertical lines mark the horizontal threshold position for amorphization (yellow) and ablation (white), which can be converted to the threshold fluences F_{am} and F_{abl}, respectively, whose values are displayed in Table 2 using the method described in the text.

Table 2
Single pulse amorphization and ablation thresholds, F_{am} and F_{abl} respectively, for irradiation at an angle of incidence θ = 54° for 400 nm, 100 fs and p-polarization. The values in brackets correspond to normal incidence (θ = 0°), extrapolated using the expression described in the text.

	c-Si	c-Ge
F_{am} (mJ/cm^2)	41 (52)	38 (51)
F_{abl} (mJ/cm^2)	172 (220)	144 (193)

3.2. Dynamics of phase transformations in Si and Ge at moderate fluences

For both materials, we have performed irradiation series with λ_{pump} = 400 nm at moderate fluences above the ablation threshold and recorded images over a wide range of different delays, from 100 fs up to 20 ns. The temporal spacing of the delays chosen is approximately logarithmically in order to account for the presence of ultrafast excitation and melting processes, as well as a considerably slower ablation onset and even slower resolidification processes. For the case of Si, a selection of normalized reflectivity images is displayed in Fig. 3(a-f), clearly showing the richness of different features corresponding to different processes. In particular, the image recorded at t = 700 fs shows a bright central ellipse surrounded by a dark ring, with the high reflectivity level being a signature of the presence of the molten phase [8–16,19,20,23,25,27,28]. The superimposed transversal reflectivity profile shows that the dark ring corresponds indeed to a reflectivity

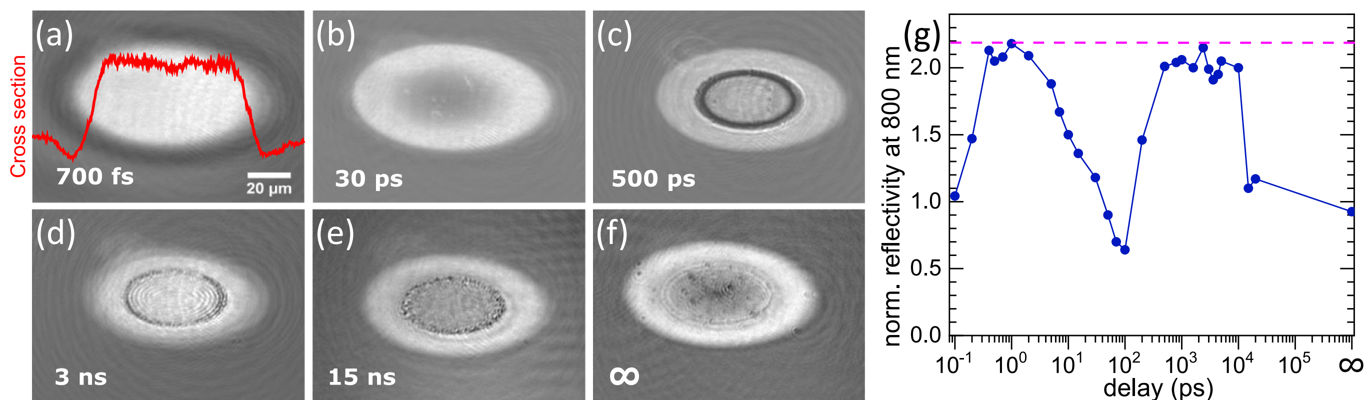

Fig. 3. (a-f) Time-resolved reflectivity images of a Si surface at a probe wavelength of 800 nm recorded at different time delays (labels) after the arrival of a 400 nm pump pulse at F = 320 mJ/cm^2, encoded in a linear gray scale with an optimized contrast. The red curve in (a) corresponds to a horizontal reflectivity profile through the spot center. The delay time "∞" in (f) corresponds to the regime of permanent modifications, recorded a few seconds after the pump pulse. (g) Evolution of the reflectivity at the spot center (area 2 x 2 μm) as a function of delay time, extracted from the complete sequence of images. The horizontal dashed line corresponds to the calculated nominal value of the reflectivity of an optically thick molten surface layer.

decrease below the initial level and that the central region has an approximately top hat reflectivity profile. Qualitatively, both features have been reported also for irradiation at 800 nm [8,24] and have been attributed to the generation of a short lived dense free electron plasma (<1 ps [27]) in the outer region (lower local fluence) and ultrafast melting in the central region due to lattice destabilization at the large number of free electrons generated (high local fluence). However, a clear difference to the corresponding results of irradiations at 800 nm at a comparable fluence (see supplemental information Fig. S1) is the much wider and more pronounced outer ring. One possible reason for this behavior is the fact that the probe wavelength for both experiment is different; λ_{probe} = 800 nm for the present case of 400 nm excitation and λ_{probe} = 400 nm for the case of 800 nm excitation (the use of different pump and probe wavelengths is necessary to suppress pump light scatter by means of spectral filtering). As reported in Ref. [25], optical probing at longer wavelengths allows a higher sensitivity to weak electron plasmas, i.e. the reflectivity decrease below the reflectivity level of the pristine material occurs at lower electron densities, reaching a minimum for 400 nm probing at $N_e = 3.4\cdot10^{22}$ cm^{-3} [24], almost five times higher than for the present case of 800 nm probing ($N_e = 7.5\cdot10^{21}$ cm^{-3}).

This initial stage of free electron generation and ultrafast melting is followed by isochoric heating to temperatures above the critical temperature to form a hot fluid at solid density [13]. Next, the liquid layer begins to expand adiabatically, which leads to a decrease in density in form of a rarefaction wave travelling into the material and leaving behind a two-phase region of liquid–gas coexistence. The first sign of this ablation process can be seen in the image recorded at t = 30 ps (Fig. 3(b)), which shows a slight darkening in the central region of the molten elliptic region. The following delays t = 500 ps – 3 ns reveal the presence of transient Newton rings, whose number increase and spacing decreases with delay. This behavior demonstrates that the ablation mechanism is based on the expansion of a semi-transparent layer with sharp interfaces [13,24]; just as for 800 nm excitation (see Fig. S1 in the supplemental information). The final structure observed in Fig. 3(f) features an ablation crater in the center, surrounded by a ring of increased reflectivity indicative of the amorphous phase, as investigated in more detail in Section 3.3.

Fig. 3(g) displays the temporal evolution of the reflectivity at the center position of the laser-excited region. An ultrafast reflectivity increase within less than 400 fs (temporal resolution of the system) due to non-thermal melting can be observed. The horizontal dashed line at R_{liquid} = 2.18 corresponds to the calculated value for an optically thick molten layer on c-Si. We attribute the fact that the values stay slightly below this values to the uncertainty in the optical properties of the liquid phase, which have been obtained via extrapolation from those reported for the visible spectral region in Ref. [20]. The reflectivity evolution shown in Fig. 3(g) then shows a continuous strong decrease (initiated at t = 2 ps down to a minimum at t = 100 ps). The origin is that the highly excited surface layer experiences isochoric heating to temperatures above the critical temperature to form a hot fluid at solid density. The subsequent adiabatic expansion of the material forms a two-phase region of liquid–gas coexistence, whose reflectivity evolution begins with an initial reflectivity decrease as a consequence of destructive interference of the probe light due to the increased layer thickness [13]. Thereafter, a constant reflectivity level near the value of the liquid phase is observed, until the effect of the solidification process can be seen at about t = 20 ns, when the propagating solid–liquid interface reaches the optical penetration depth of the probe light, leading to a rapid decrease of the reflectivity [20].

Besides the above-mentioned difference in the width of the ring upon excitation at 400 nm (c.g. Fig. 3(a)) compared to excitation at 800 nm excitation (Fig. S1(a)), the dynamics of the triggered phase transitions show little difference. This is an important finding, since the excitation conditions differ strongly for the two wavelengths. In particular, in the present case of λ_{pump} = 400 nm, the optical penetration depth is $OPD_{Si\ (400\ nm)}$ = 73 nm, which would suggest a purely linear absorption mechanism. In contrast, the very large value for λ_{pump} = 800 nm, $OPD_{Si\ (800\ nm)}$ = 9.75 μm leads to a situation where absorption is dominated by to a two-photon absorption (TPA) mechanism, in line with the results reported in [26,27], where dominant TPA has been demonstrated for excitation at 620 nm ($OPD_{Si(620\ nm)}$ = 2.93 μm). Thus, the different linearity of the absorption mechanisms at λ_{pump} = 400 nm and λ_{pump} = 800 nm might lead to a difference in the lateral electron density profiles for a Gaussian intensity distribution. While such difference might indeed be visible in the data, showing a wider dark ring for 400 nm excitation at t = 700 fs, the difference could also be attributed to the higher sensitivity of the probe wavelength (λ_{probe} = 800 nm), as discussed earlier. Yet, more information is needed in order to conclude on the responsible mechanism.

To this end, an equivalent study has been performed for Ge and the results are displayed in Fig. 4. The evolution of the reflectivity in the spot center (c.f. Fig. 4(g)) displays qualitatively the same behavior as observed for Si in Fig. 3(g): An ultrafast reflectivity rise due to non-thermal melting, followed by a strong decrease due to the onset of ablation, with the minimum shifted to slightly longer times. The latter fact can be attributed to the increased energy deposition in Ge at similar fluences due to the higher absorption coefficient (see Table 1), consistent with a wider crater (Fig. 4f) than that observed in Si (Fig. 3f). Besides, a comparison of the corresponding normalized reflectivity images to those of Si shown in Fig. 3 reveals three additional differences. First,

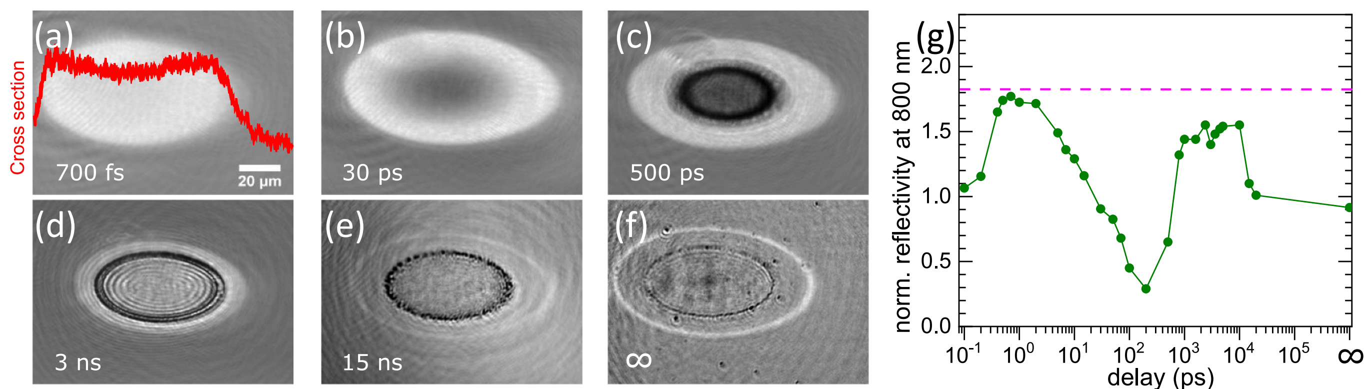

Fig. 4. (a-f) Reflectivity images of a Ge surface at a probe wavelength of 800 nm recorded at different time delays (labels) after the arrival of a 400 nm pump pulse at F = 340 mJ/cm^2, encoded in a linear gray scale with an optimized contrast. The red curve in (a) corresponds to a horizontal reflectivity profile through the spot center. The delay time "∞" in (f) corresponds to the regime of permanent modifications, recorded a few seconds after the pump pulse. (g) Evolution of the reflectivity at the spot center as a function of delay time, extracted from the complete sequence of images. The horizontal dashed line corresponds to the calculated nominal value of the reflectivity of an optically thick molten surface layer on c-Ge.

the outer ring structure of reduced reflectivity due to a free electron plasma a delay of $t = 700$ fs (Fig. 4(a)) is less pronounced than for Si at this delay (c.f. Fig. 3(a)). Second, the higher modulation depth of the Newton rings in the corresponding temporal range ($t = 500$ ps and $t = 3$ ns), which can be attributed to the different optical properties of Si and Ge at the probe wavelength (displayed in Table 1). It should be said, though, that the number of rings at a given delay is almost the same, which indicates a similar velocity of the ablating layer. Third, the final structure at $t = \infty$ displays only a very thin outer ring of increased reflectivity corresponding to the amorphous phase compared to a much wider ring for the case of Si (see Fig. 3(f)). This fact demonstrates that the amorphization window of Ge at $\lambda_{pump} = 400$ nm is much more narrow than for Si. An equivalent observation can be made for $\lambda_{pump} = 800$ nm (see suppl. information Figs. S1(f) and S2(f)), where no amorphization at all occurs for Ge and only weak amorphization in Si. A more detailed discussion and data analysis of amorphization in the two materials is performed in Section 3.3.

3.3. Thickness of the amorphized surface layer

In order to determine the thickness of the amorphous layer in semiconductors, conventional optical microscopy with monochromatic illumination can be used [22,28]. The light reflected at the material surface interferes with the light reflected at the embedded crystalline/amorphous interface, leading to intensity modulations that depend on the layer thickness. The layer thickness at each position can be calculated by a simple optical multilayer model, using the optical properties of the two material phases at the illumination wavelengths.

Fig. 5 displays the results obtained for Si. The two images correspond to the same laser-irradiated surface region in its final state ($t = \infty$), but have been recorded at different illumination wavelength, $\lambda_{illum} = 460$ nm in (a) and $\lambda_{illum} = 800$ nm in (b). The striking differences in the width of the bright and dark rings for both wavelengths is a direct consequence of the above-explained interference scenario of a thin amorphous layer on top of a crystalline substrate, since shorter a illumination wavelength leads to a larger number of interference oscillations for a given thickness than longer wavelengths. This wavelength-dependent oscillation period can be seen directly by the corresponding calculations for the two different wavelengths, displayed in Fig. 5(c), showing the calculated reflectivity evolution of Si as a function of the thickness of an amorphous top layer. An estimation of the maximum thickness of the surface layer achieved can be performed straight–forward by counting the number of reflectivity maxima and minima observed experimentally in the spot, starting from outside the spot and moving towards the crater rim. For $\lambda_{illum} = 460$ nm, this yields the sequence maximum-

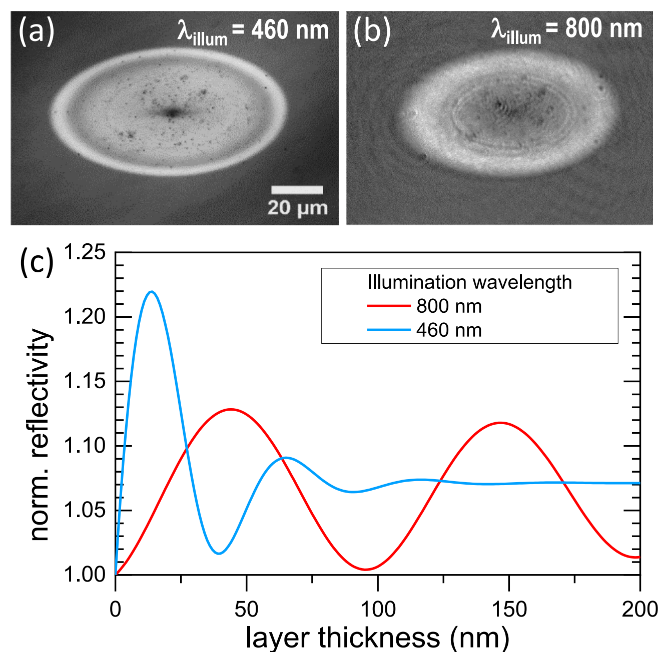

Fig. 5. Optical microscopy images of the Si surface after irradiation under the conditions as those of Figs. 2 and 3 ($\lambda_{pump} = 400$ nm), using illumination at (a) 460 nm and (b) 800 nm. (c) Calculated evolution of the normalized reflectivity for different wavelengths as a function of thickness of an amorphous top layer on a crystalline substrate.

minimum–maximum, indicating a thickness of $d_{a\text{-}Si400nm} \approx 70$ nm in the corresponding reflectivity curve. This estimation is consistent with the result obtained for $\lambda_{illum} = 800$ nm illumination, yielding only one maximum and the onset of a reflectivity decrease when approaching the crater rim, which indicates a similar thickness. Yet, these results are different from those reported by Izawa et al. for irradiation at 400 nm and a similar pulse duration [16]. The authors reported a maximum thickness of only 17 nm. Considering the similar fluence thresholds observed in their work and ours (see section 3.1) the origin of this strong difference is unclear.

The considerable thickness of the amorphous layer observed in our work for $\lambda_{pump} = 400$ nm irradiation, is in strong contrast to the results observed for irradiation at $\lambda_{pump} = 800$ nm, for which only very weak signs of the presence of the amorphous phase were observed (see Fig. S1 (f)). For the latter case, it has been shown that irradiation with multiple

laser pulses is required for the formation of the amorphous phase [29]. The fact that single pulse amorphization can be achieved for excitation at 400 nm is line with the results reported in [6] and can be attributed to the different absorption mechanism, leading to stronger thermal gradients and thus faster solidification velocities.

The same investigation on the presence and thickness of an amorphous layer after irradiation has been performed for the irradiations preformed in Ge, shown in Fig. 6. Also here, a clear permanent reflectivity increase is observed at both illumination wavelength, (a) 460 nm and (b) 800 nm; but it is confined to a very narrow ring surrounding the crater. The differences between the two images recorded are quite subtle. It is worth emphasizing that the calculated reflectivity evolution $\lambda_{illum} = 460$ nm does not predict a second maximum as for the case of Si, but saturates after the decrease from the first maximum. This behavior prevents a precise prediction of the maximum layer thickness for this illumination wavelength. Yet a reasonable estimation can be done by comparing the experimental reflectivity increase and decrease for $\lambda_{illum} = 800$ nm, featuring a bright ring followed by a decrease to almost the initial reflectivity. Comparing this behaviour to the corresponding calculated reflectivity evolution as a function of thickness indicates a thickness of $d_{a\text{-}Ge400nm} \approx 70$ nm, which is similar to the one obtained for Si. In turn, for excitation at $\lambda_{pump} = 800$ nm, no signs of amorphization have observed as shown in the supplemental information (Fig. S2), consistent with the results reported in Refs. [14,15]. This fundamental difference in the final state obtained in Ge after irradiation for different excitation wavelength can be attributed to the extremely short optical penetration depth at 400 nm excitation ($OPD_{Ge(400\ nm)} = 14$ nm), leading to steep temperature gradients, strong undercooling and thus much faster solidification speeds than for 800 nm excitation, preventing the atoms to occupy the tetrahedral lattice position of the crystalline phase.

3.4. Phase transformations in the high fluence regime: Recoil pressure effects

In order to investigate the possible presence of additional mechanisms at extreme excitation levels, we have performed a complete study of the transient reflectivity changes in the very high fluence regime for $\lambda_{pump} = 400$ nm, more than a factor of 30 above the ablation threshold. At first glance, most of the dynamics of the observed reflectivity changes in the spot center (c.f. Fig. 7(c + d)) is very similar to the moderate fluence regime, both for Si and Ge. Also here, an ultrafast rise of the reflectivity due to non-thermal melting is followed by a rapid decrease due to the onset of ablation. Yet the minimum of this decrease is obtained within much shorter times ($t_{min,high} \approx 20$ ps) compared to excitation at moderate fluences ($t_{min,mod} \approx 100$–200 ps). This pronounced difference is an indication of the much higher energy deposition within the laser pulse duration, triggering a much faster expansion of the ablating layer. Consistently, the recovery of the surface reflectivity is much slower, reaching values close to the liquid phase at delays times of 10 ns or longer.

In this context we would like to draw attention to the fact that in this delay range of around $t = 10$ ns, the experimental reflectivity values lie ~~significantly~~ above the values of the liquid phase, both for Si and Ge, as can be appreciated in Fig. 7(c,d). Moreover, the measured transient values do not only exceed the calculated values of the liquid phase of both materials, which could contain errors due to the precision of the optical properties of the liquid phase reported in Ref. [20]. They also exceed the experimentally observed values of the molten phase in the moderate excitation regime at times soon after the formation of the molten phase (i.e. either after non-thermal melting or after electron–phonon coupling), as can be clearly observed by comparing the data of Fig. 7(c-d) to Fig. 3(g) and Fig. 4(g).

A similar behavior has been reported for Ge upon excitation with picosecond laser at 583 nm wavelength at fluences more than 10x above the melting threshold [30], using real-time reflectivity measurements employing a streak camera and a probe wavelength of 514 nm. In that work, the authors observed an extraordinarily high and constant transient reflectivity over fluence regime ranging from 11 – 25 times the melting threshold. The authors attributed this high reflectivity level to a new structural state of the liquid phase of Ge remaining at the surface, induced by the high pressure exerted by the ablating material. The fact that our data also shows experimental reflectivity values significantly above the value of that corresponding to the liquid phase points to a similar mechanism and the presence of a pressure-induced phase transition. Moreover, the transient reflectivity images at the delay times that correspond to this temporal region (shown in Fig. 7(a, e)) clearly reveal an elliptical central region, spatially distinguished from the surrounding ring. This relatively sharp spatial separation from the outer annular rings of lower local fluence could be an indication of a transition from the molten phase with the well-known properties to a highly compressed liquid phase with different optical properties.

In addition, the characteristic signature of a radially expanding shockwave in air can be appreciated in the images in form of an annular dark ring structure well outside the laser excited region. A further indication of the extreme conditions in terms of temperature and pressure are the bubble-like features in the spot center and ejected material particles outside that can be seen after irradiation (see Fig. 7(b,e)). It has to be said, though, that experimental time-resolved studies with structural sensitivity, such as ultrafast X-ray diffraction upon fs laser excitation at such high fluences, would be necessary to confirm our hypothesis of a pressure-induced liquid–liquid phase transition at long delay times. Such a study has recently demonstrated the existence of a liquid–liquid phase transition of different origin in the phase change materials $Ag_4In_3Sb_{67}Te_{26}$ and $Ge_{15}Sb_{85}$ within a time window from a few ps up to a few ns, induced at fluences well below the ablation threshold [31].

4. Conclusions

We have investigated transient and permanent changes induced in crystalline Si and Ge upon irradiation with single 400 nm, 100 fs laser pulses at moderate to high peak fluences. The amorphization threshold fluences for p-polarized light at angle of incidence of 54° were determined as $F_{am}(\text{Si}) = 41$ mJ/cm^2 and $F_{am}(\text{Ge}) = 38$ mJ/cm^2; the ablation

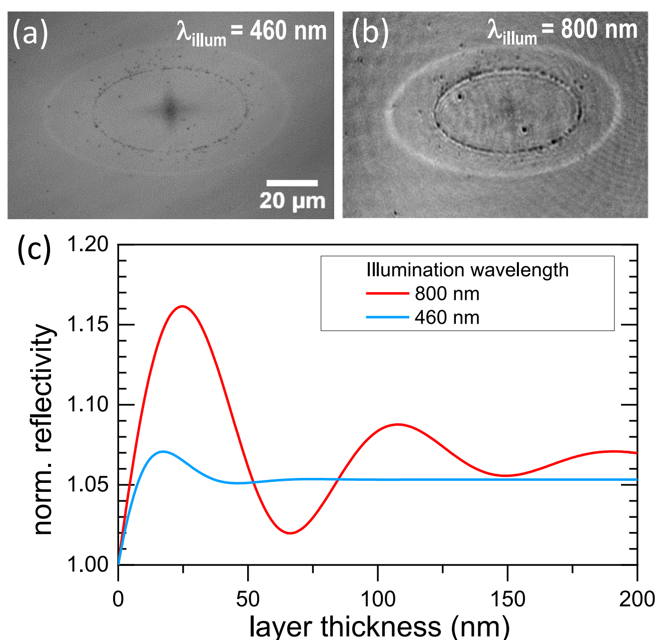

Fig. 6. Optical microscopy images of the Ge surface after irradiation under the conditions shown in Figs. 2 and 4, using illumination at (a) 460 nm and (b) 800 nm. (c) Calculated evolution of the reflectivity for different wavelengths as a function of thickness of an amorphous top layer on a crystalline substrate.

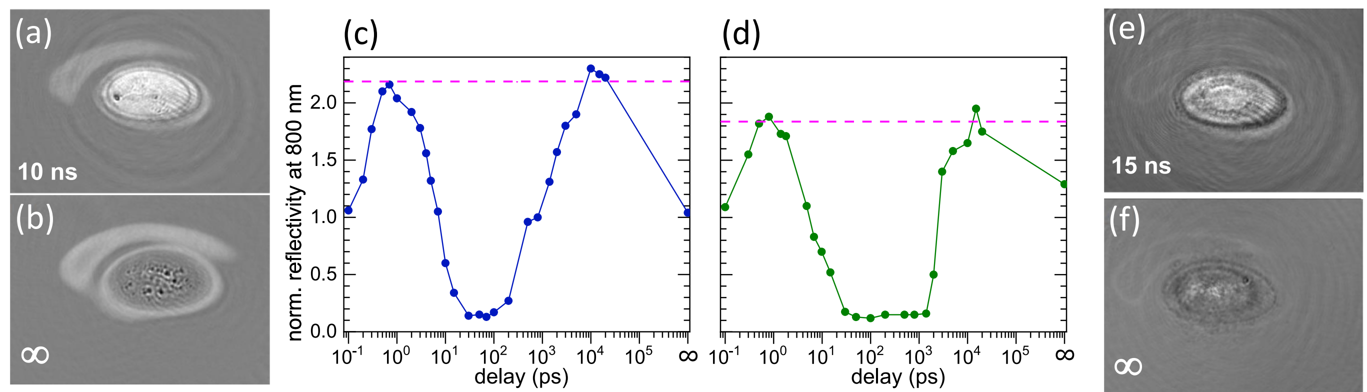

Fig. 7. Reflectivity images recorded at a probe wavelength of 800 nm at different time delays (labels) after the arrival of a 400 nm pump pulse for (a,b) Si at F = 6.0 J/cm^2 and (e,f) Ge at F = 5.8 J/cm^2 The delay time "∞" in (b) and (f) corresponds to the regime of permanent modifications, recorded a few seconds after the pump pulse. (c, d) Evolution or the reflectivity of the spot center as a function of delay time, extracted from the complete sequence of images for Si (c) and Ge (d). The horizontal dashed line corresponds to the calculated nominal value of the reflectivity of an optically thick molten surface layer.

threshold values as F_{abl}(Si) = 172 mJ/cm^2 and F_{abl}(Ge) = 144 mJ/cm^2. Concerning the transformation dynamics at moderate fluences above the ablation threshold, the transient reflectivity images recorded for Ge and Si display the entire sequence of laser-induced processes, starting from the generation of a free-electron plasma, non-thermal melting, ablation onset and expansion of a semi-transparent ablation layer with sharp interfaces, whose velocity can be determined from the data. The observed dynamics is similar to the behavior reported in literature upon excitation at 800 nm, which is rather unexpected due to the extremely different excitation conditions, namely linear optical penetration depth that differ by several orders of magnitude. It is also found that amorphous surface layers with a thickness of around 70 nm are formed upon irradiation at 400 nm in both materials, whereas no or little amorphization is observed at 800 nm. We attribute this difference to the shorter absorption depth, yielding higher temperature gradients and larger undercoolings.

Finally, at excitation with peak fluences more than 30 times the ablation threshold, the surface of both materials obtains an anomalous high-reflectivity at around 10 ns that cannot be explained by the molten phase. We speculate that at under these conditions a transient, recoil pressure induced liquid–liquid phase transition might be induced as reported previously for Ge upon high fluence ps laser excitation. Yet, experiments with time-resolved structural probe techniques would be required to validate this hypothesis.

CRediT authorship contribution statement

Daniel Puerto: Writing – review & editing, Visualization, Methodology, Investigation, Formal analysis, Data curation, Conceptualization. **Javier Solis:** Writing – review & editing, Project administration, Funding acquisition. **Jan Siegel:** Writing – original draft, Supervision, Methodology, Investigation, Funding acquisition, Conceptualization.

Declaration of competing interest

The authors declare the following financial interests/personal relationships which may be considered as potential competing interests: Jan Siegel reports financial support was provided by Ministry of Science and Innovation/State Agency of Investigation. Jan Siegel reports financial support was provided by the European Union NextGenerationEU/PRTR. Daniel Puerto reports financial support was provided by Government of Valencia. If there are other authors, they declare that they have no known competing financial interests or personal relationships that could have appeared to influence the work reported in this paper.

Data availability

Data will be made available on request.

Acknowledgements

This work is part of the projects TEC2008-001183, PID2020-112770RB-C21 and TED2021-130894B-C22 and has been financed by MCIN/AEI/10.13039/501100011033 (Ministry of Science and Innovation/State Agency of Investigation) and European Union NextGenerationEU/PRTR, as well as by the "Generalitat Valenciana" (project PROMETEO/2021/006).

Appendix A. Supplementary material

Supplementary data to this article can be found online at https://doi.org/10.1016/j.apsusc.2024.160372.

References

[1] L. Pavesi, Thirty years in silicon photonics: a personal view, Front. Phys. 9 (2021) 1–30, https://doi.org/10.3389/fphy.2021.786028.
[2] V.R. Almeida, C.A. Barrios, R.R. Panepucci, M. Lipson, All-optical control of light on a silicon chip, Nature 431 (2004) 1081–1084, https://doi.org/10.1038/nature02921.
[3] P.L. Liu, R. Yen, N. Bloembergen, R.T. Hodgson, Picosecond laser-induced melting and resolidification morphology on Si, Appl. Phys. Lett. 34 (1979) 864–866, https://doi.org/10.1063/1.90703.
[4] M. Wuttig, H. Bhaskaran, T. Taubner, Phase-change materials for non-volatile photonic applications, Nat. Photonics 11 (2017) 465–476, https://doi.org/10.1038/nphoton.2017.126.
[5] X. Li, R. Li, Z. Yu, J. Xing, W. Kong, Y. Wang, J. Yang, Deepening of nanograting structures on Si by a two-step laser spatial-selective amorphization strategy combined with chemical etching, Appl. Surf. Sci. 589 (2022) 152965, https://doi.org/10.1016/J.APSUSC.2022.152965.
[6] M. Garcia-Lechuga, N. Casquero, A. Wang, D. Grojo, J. Siegel, Deep silicon amorphization induced by femtosecond laser pulses up to the mid-infrared, Adv. Opt. Mater. 9 (2021) 2100400, https://doi.org/10.1002/adom.202100400.
[7] Y. Borodaenko, S. Syubaev, S. Gurbatov, A. Zhizhchenko, A. Porfirev, S. Khonina, E. Mitsai, A.V. Gerasimenko, A. Shevlyagin, E. Modin, S. Juodkazis, E.L. Gurevich, A.A. Kuchmizhak, Deep subwavelength laser-induced periodic surface structures on silicon as a novel multifunctional biosensing platform, ACS Appl. Mater. Interfaces 13 (2021) 54551–54560, https://doi.org/10.1021/ACSAMI.1C16249/SUPPL_FILE/AM1C16249_SI_001.PDF.
[8] P. Kühler, D. Puerto, M. Mosbacher, P. Leiderer, F.J. Garcia de Abajo, J. Siegel, J. Solis, Femtosecond-resolved ablation dynamics of Si in the near field of a small dielectric particle, Beilstein J. Nanotechnol. 4 (2013) 501–509, https://doi.org/10.3762/bjnano.4.59.
[9] M. Garcia-Lechuga, J. Solis, J. Siegel, Probing Matter by Light, in: R. Stoian, J. Bonse (Eds.), Ultrafast Laser Nanostructuring, Springer Cham, 2023: pp. 277–319. doi: 10.1007/978-3-031-14752-4_7.
[10] J. Winter, S. Rapp, M. Spellauge, C. Eulenkamp, M. Schmidt, H.P. Huber, Ultrafast pump-probe ellipsometry and microscopy reveal the surface dynamics of

femtosecond laser ablation of aluminium and stainless steel, Appl. Surf. Sci. 511 (2020) 145514, https://doi.org/10.1016/j.apsusc.2020.145514.
[11] C. Shank, R. Yen, C. Hirlimann, Time-resolved reflectivity measurements of femtosecond-optical-pulse-induced phase transitions in silicon, Phys. Rev. Lett. 50 (1983) 454–457, https://doi.org/10.1103/PhysRevLett.50.454.
[12] M.C. Downer, R.L. Fork, C.V. Shank, Femtosecond imaging of melting and evaporation at a photoexcited silicon surface, J. Opt. Soc. Am. B 2 (1985) 595–599, https://doi.org/10.1364/JOSAB.2.000595.
[13] K. Sokolowski-Tinten, J. Bialkowski, A. Cavalleri, D. von der Linde, A. Oparin, J. Meyer-ter-Vehn, S.I. Anisimov, Transient states of matter during short pulse laser ablation, Phys. Rev. Lett. 81 (1998) 224–227, https://doi.org/10.1103/PhysRevLett.81.224.
[14] J. Bonse, G. Bachelier, J. Siegel, J. Solis, Time- and space-resolved dynamics of melting, ablation, and solidification phenomena induced by femtosecond laser pulses in germanium, Phys. Rev. B 74 (2006) 134106, https://doi.org/10.1103/PhysRevB.74.134106.
[15] N. Casquero, C. Ruiz de Galarreta, Y. Fuentes-Edfuf, J. Solis, C.D. Wright, J. Siegel, Propagation dynamics of the solid–liquid interface in Ge upon ns and fs laser irradiation, J. Phys. D Appl. Phys. 55 (2022) 365104, https://doi.org/10.1088/1361-6463/ac791e.
[16] Y. Izawa, Y. Izawa, Y. Setsuhara, M. Hashida, M. Fujita, R. Sasaki, H. Nagai, M. Yoshida, Ultrathin amorphous Si layer formation by femtosecond laser pulse irradiation, Appl. Phys. Lett. 90 (2007) 19–21, https://doi.org/10.1063/1.2431709.
[17] J.M. Liu, Simple technique for measurements of pulsed Gaussian-beam spot sizes, Opt. Lett. 7 (1982) 196–198.
[18] D.E. Aspnes, Dielectric functions and optical parameters of Si, Ge, GaP, GaAs, GaSb, InP, InAs, and InSb from 1.5 to 6.0 eV, Phys Rev B 27 (1983) 985. doi: 10.1111/j.1468-0130.2010.00653.x.
[19] E.D. Palik, Handbook of optical constants of solids, Elsevier Inc., 2012. doi: 10.1016/C2009-0-20920-2.
[20] G.E. Jellison, D.H. Lowndes, Measurements of the optical properties of liquid silicon and germanium using nanosecond time-resolved ellipsometry, Appl. Phys. Lett. 51 (1987) 352–354, https://doi.org/10.1063/1.98438.
[21] Y. Fuentes-Edfuf, M. Garcia-Lechuga, J. Solis, J. Siegel, Ultrafast electron dynamics and optical interference tomography of laser excited steel, Laser Photon Rev 16 (2022) 2200511, https://doi.org/10.1002/lpor.202200511.
[22] J. Bonse, K.W. Brzezinka, A.J. Meixner, Modifying single-crystalline silicon by femtosecond laser pulses: an analysis by micro Raman spectroscopy, scanning laser microscopy and atomic force microscopy, Appl. Surf. Sci. 221 (2004) 215–230, https://doi.org/10.1016/S0169-4332(03)00881-X.
[23] J. Bonse, S.M. Wiggins, J. Solis, Dynamics of phase transitions induced by femtosecond laser pulse irradiation of indium phosphide, Appl. Phys. A 80 (2005) 243–248, https://doi.org/10.1007/s00339-004-3025-z.
[24] M. Garcia-Lechuga, D. Puerto, Y. Fuentes-Edfuf, J. Solis, J. Siegel, Ultrafast moving-spot microscopy: birth and growth of laser-induced periodic surface structures, ACS Photonics 3 (2016) 1961–1967, https://doi.org/10.1021/acsphotonics.6b00514.
[25] M. Garcia-Lechuga, J. Solis, J. Siegel, Key stages of material expansion in dielectrics upon femtosecond laser ablation revealed by double-color illumination time-resolved microscopy, Appl. Phys. A 124 (2018) 221, https://doi.org/10.1007/s00339-018-1650-1.
[26] D.H. Reitze, T.R. Zhang, M. Wm, M.C.D. Wood, Two-photon spectroscopy of silicon using femtosecond pulses at above-gap frequencies, J. Opt. Soc. Am. B 7 (1990) 84, https://doi.org/10.1364/josab.7.000084.
[27] K. Sokolowski-Tinten, D. Von Der Linde, Generation of dense electron-hole plasmas in silicon, Phys. Rev. B 61 (2000) 2643–2650, https://doi.org/10.1103/PhysRevB.61.2643.
[28] Y. Fuentes-Edfuf, M. Garcia-Lechuga, D. Puerto, C. Florian, A. Garcia-Leis, S. Sanchez-Cortes, J. Solis, J. Siegel, Coherent scatter-controlled phase-change grating structures in silicon using femtosecond laser pulses, Sci. Rep. 7 (2017) 4594, https://doi.org/10.1038/s41598-017-04891-3.
[29] Y. Fuentes-Edfuf, M. Garcia-Lechuga, D. Puerto, C. Florian, A. Garcia-Leis, S. Sanchez-Cortes, J. Solis, J. Siegel, Fabrication of amorphous micro-ring arrays in crystalline silicon using ultrashort laser pulses, Appl. Phys. Lett. 110 (2017) 211602, https://doi.org/10.1063/1.4984110.
[30] N. Chaoui, J. Siegel, S.M. Wiggins, J. Solis, Pressure-induced transient structural change of liquid germanium induced by high-energy picosecond laser pulses, Appl. Phys. Lett. 86 (2005) 1–3, https://doi.org/10.1063/1.1940117.
[31] P. Zalden, F. Quirin, M. Schumacher, J. Siegel, S. Wei, A. Koc, M. Nicoul, M. Trigo, P. Andreasson, H. Enquist, M.J. Shu, T. Pardini, M. Chollet, D. Zhu, H. Lemke, I. Ronneberger, J. Larsson, A.M. Lindenberg, H.E. Fischer, S. Hau-Riege, D.A. Reis, R. Mazzarello, M. Wuttig, K. Sokolowski-Tinten, Femtosecond x-ray diffraction reveals a liquid–liquid phase transition in phase-change materials, Science 364 (2019) (1979) 1062–1067, https://doi.org/10.1126/science.aaw1773.